ESC European Society of Cardiology

Cardiovascular Research (2026) **00**, 1–14
https://doi.org/10.1093/cvr/cvaf279

Identification of rare missense variants reducing cathepsin O secretion in families with intracranial aneurysm

Milène Fréneau[1†], Raphael Blanchet[1†], Maxence Bodet[1], Sandro Benichi [1], Mary-Adel Mrad[1], Surya Prakash Rao Batta [1], Marc Rio [1], Stéphanie Bonnaud[1], Pierre Lindenbaum [1], Fabien Laporte [1], Stéphane Cuénot [2], Thibaud Quillard [1], Mike Maillasson [3], Sandrine Morel [4,5], Brenda R. Kwak [4], Philippe Bijlenga [5], Jean-François Deleuze [6], Christian Dina [1], Stéphanie Chatel[1], Emmanuelle Bourcereau[7], Solène Jouan[7], Arturo Consoli[8], Cyril Dargazanli [9], Julien Ognard [10], ICAN Study Group, Hubert Desal [1,7], Anne-Clémence Vion [1], Romain Bourcier [1,7†], Gervaise Loirand [1*†], and Richard Redon [1*†]

[1]Nantes Université, CHU Nantes, CNRS, INSERM, l'institut du thorax, F-44000 Nantes, France; [2]Nantes Université, CNRS, Institut des Matériaux Jean Rouxel, IMN, F-44000 Nantes, France; [3]Nantes Université, CNRS, INSERM, BioCore, F-44000 Nantes, France; [4]Department of Pathology and Immunology, Faculty of Medicine, University of Geneva, CH-1211 Geneva, Switzerland; [5]Neurosurgery Division, Department of Clinical Neurosciences, Faculty of Medicine, Geneva University Hospitals and University of Geneva, Geneva, Switzerland; [6]CEA, Centre National de Recherche en Génomique Humaine (CNRGH), Université Paris-Saclay, F-91057 Evry, France; [7]Department of Neuroradiology, CHU Nantes, F-44000 Nantes, France; [8]Department of Interventional Neuroradiology, Foch Hospital, University Versailles Saint-Quentin en Yvelines, F-92073 Suresnes, France; [9]Department of Neuroradiology, University Hospital Centre Montpellier, F-34000 Montpellier, France; and [10]Radiology Department, University Hospital, F-29000 Brest, France

Received 29 September 2025; accepted 18 October 2025; online publish-ahead-of-print 9 January 2026

Aims

Intracranial aneurysm (IA) is a common cerebrovascular abnormality characterized by localized dilation and wall thinning in cerebral arteries, which can rupture and lead to fatal subarachnoid haemorrhage. Although genetic factors can contribute to IA, the genetic pre-disposition of IA is largely unknown. This study aims to identify rare functional variants associated with IA in families with multiple affected subjects and explore their impact on IA pathophysiology.

Methods and results

By combining whole-exome sequencing and identity-by-descent analyses, we have identified two rare missense variants in the CTSO gene associated to IA in two large families with multiple affected subjects. We found that the cysteine-type papain-like cathepsin O (CTSO) encoded by *CTSO* is expressed in the circle of Willis of mice and in the wall of human IA domes. Stretching of vascular smooth muscle cells (VSMC) induced CTSO secretion. CTSO controls VSMC migration and adhesion to the extracellular matrix, and directly interacts with fibronectin (FN). CTSO depletion, or expression of the two CTSO variants, which are poorly secreted, increased the amount of FN. Moreover, CTSO depletion augmented VSMC stiffness, which was reduced by the addition of exogenous CTSO.

Conclusion

Collectively, our findings identify CTSO as a potential new player in arterial remodelling, regulating FN deposition and VSMC function, supporting the causal role of rare coding CTSO variants in familial forms of IA.

Keywords

Genetics • Intracranial aneurysm • Cathepsin • Cerebral artery • Smooth muscle • Extracellular matrix • Fibronectin • Stiffness

* Corresponding author. Tel: +33 228 08 01 16; fax: +33 228 08 01 30, E-mail: gervaise.loirand@univ-nantes.fr (G.L.); E-mail: richard.redon@univ-nantes.fr (R.R.)
† These authors contributed equally to this work as first and last authors.

1. Introduction

Intracranial aneurysm (IA) is a generally asymptomatic localized dilation associated with thinning and structural defects of the intracranial arterial wall affecting 1–5% of the general population.[1] The main risk of IA is its unpredictable rupture, responsible for ∼36 000 of subarachnoid haemorrhage cases per year in Europe and a major cause of sudden death in 'young healthy' subjects, in particular in women (peak of age: 50–60 years).[2] Although hypertension, ageing, female sex, smoking, excessive alcohol consumption, and family history of IA have been identified as risk factors predisposing to IA, the mechanisms underlying IA formation, growth, and rupture are mostly unknown. However, local haemodynamic constraints of shear stress and pressure are assumed to play a key role.[3] The aggregation of patients in IA families suggests that genetic factors contribute to disease susceptibility, and identifying these factors might be beneficial for at-risk patients before IA rupture.[4] Genome-wide association studies have identified several common risk loci associated with IA.[5] However, the identification of specific genes or causal molecular pathways remains largely inconclusive and these common alleles together only explain a small fraction of the risk attributable to genetics for IA in the general population. On the other hand, whole-exome sequencing (WES) has the potential to detect rare coding variants that have large effect and induce a high risk of developing IA. Identifying such variants also could provide valuable insights into IA pathophysiology and pave the way for new diagnostic or therapeutic strategies. Indeed, recent studies have demonstrated the usefulness of familial approaches based on WES to improve knowledge on the molecular mechanisms underlying IA formation and rupture from the discovery of rare predisposing variants such as *RNF213*,[6] *THSD1*,[7] *LOXL2*,[8] *PCNT*,[9] *ARHGEF17*,[10] *ANGPTL6*,[11] and *PPIL4*.[12]

In the present study, by combining WES and identity-by-descent (IBD) analysis, we identified rare coding variants in the Cathepsin O gene (*CTSO* [MIM: 600550]) in two familial cases of IA. CTSO is one of the 11 cysteine-type papain-like cathepsins identified in humans about which almost nothing is known.[13] Here we report that CTSO is expressed in the arterial wall of the circle of Willis in mice and in the wall of human IA domes. Our functional analysis revealed that CTSO controls vascular smooth muscle cell (VSMC) migration and adhesion to the extracellular matrix (ECM), and directly interacts with fibronectin (FN). Furthermore, CTSO depletion increased VSMC stiffness. These findings suggest that the increased susceptibility to IA induced by *CTSO* variants is likely related to their primary effects on vascular tissue, and more particularly on the media layer of the wall of cerebral arteries.

2. Methods

2.1 Study approval

For genetic analysis, index case subjects with IA and their relatives were recruited following the French ethical guidelines for genetic research and under approval from the French Ministry of Research and the local ethical committee (no. DC-2011-1399; Clinical Trial NCT02712892). Informed written consent was obtained from each individual agreeing to participate in the genetic study, to whom MRI screening and blood sampling were proposed. AneuX biobank was approved by the Geneva State Ethics Commission for Research involving humans (Geneva CCER 2022-00426). All patients approved for the use of their data and biological samples in the field of cerebrovascular research. Research was conducted in accordance with the Declaration of Helsinki.

2.2 Clinical recruitment

Familial cases of IA are defined as at least two first-degree relatives both diagnosed with typical IA (defined as a saccular arterial dilatation of any size occurring at a bifurcation of the intracranial vasculature), without any age limitation. Index case subjects and their relatives were recruited according to a recruitment process previously described.[14] Neuroradiological phenotyping was performed in each recruiting centre by interventional neuroradiologists, neurologists, and neurosurgeons in order to recruit only case subjects with typical saccular bifurcation IA. Mycotic, fusiform-shaped, or dissecting IAs were systematically excluded, as well as IA in relation with an arteriovenous malformation and IA resulting from syndromic disorders such as Marfan disease or vascular forms of Elhers Danlos. For all included patients we recorded the date of birth, if IA, the cases of rupture, the number of IA, the IA larger diameter in mm, the IA locations according to the four following groups internal carotid artery (ICA), posterior cerebral circulation (PCA), middle cerebral artery (MCA) or anterior cerebral artery (ACA), the smoking habits, the history of high blood pressure and ischaemic stroke, the level of alcohol intake per week, the history of diabetes or dyslipidemia, obesity (BMI > 30), treatment by statin, antiplatelet, oral anticoagulant, and anti-inflammatory drugs.

2.3 Whole-exome sequencing

Genomic DNA was extracted from peripheral blood lymphocytes using the NucleoSpin Blood kit XL (Macherey Nagel). Whole-exome fragments were captured with the SureSelect Human All Exon V4 kit (Agilent technology), according to manufacturer protocol. Alignment on reference genome (Broad Institute human_g1k_v37) was performed using Burrow-Wheeler aligner (Bwa mem v0.7.10).[15] Picard v1.119 was used to flag duplicates and recalibration was achieved through GATK v3.2.2 (broadinstitute, 2023).[16] Variants were called with GATK HaplotypeCaller on all exons hg19 exons (NCBI RefSeq), annotated with SnpEff and vcfGnomad (jvarkit) using gnomad v2.1.[17] Quality filters detailed in the Supplementary material online, *Table S1* were applied. Only variants annotated as non-synonymous or affecting splicing, and reported with a minor allelic frequency (MAF) below 0.1% in the non-Finnish European (NFE) population (64 603 individuals reported in gnomAD v2.1, based on 56 885 whole-exome and 7718 whole-genome sequences), were subsequently considered.

2.4 IBD analysis

Haplotype sharing between affected relatives were identified through IBD analysis based on SNP genotyping data. Fluorescence intensities were obtained from Precision Medicine Research Array (PMRA—Affymetrix) and quantified by Affymetrix GeneTitan Multi-Channel Instrument. Genotypes of affected relatives II.2, II9, III.2, III.4, and III.7 were merged with PREGO control population[18] and SNPs with MAF < 10%, call rate <95% or $P <$ 1.10–5 when testing for Hardy–Weinberg equilibrium were excluded. IBD regions were then identified using IBDLD v3.34 with noLD method.[19] Familial segregation analysis by capillary sequencing was performed on an Applied Biosystems 3730 DNA Analyzer, using standard procedures. Sequence analyses were performed with SeqScape v.2.5.

2.5 Human saccular IA samples

Saccular IA samples are from the Aneux Biobank.[20] All samples were obtained during microsurgery by resection of the IA dome (i.e. the bulging region of the IA) after clipping of the neck performed at the Division of Neurosurgery of the Geneva University Hospitals, Switzerland. IAs were stored as previously described,[20] fixed in formol, embedded in paraffin, sectioned at 5 µm, and conserved at 4°C until immunohistochemical staining is performed.

2.6 Immunohistochemical staining of CTSO on human saccular IA samples

Labelling of IA sections was performed following heat-induced epitope retrieval in citrate buffer (10 mM, pH 6.0). Sections of unruptured ($n = 10$) and ruptured ($n = 10$) IA were immunolabeled with the Prestige Antibodies® antibody recognizing CTSO (HPA002041, Sigma–Aldrich). Negative controls were performed without CTSO antibody. Haematoxylin and eosin were used as counterstaining. Image acquisition of immunohistochemical staining of CTSO was done with a whole-slide scanner NanoZoomer (Hamamatsu). Total tissue area and positive staining area

were quantified using Image-Pro Plus (Media Cybernetics), and the positive CTSO staining was expressed relative to total sample area.

2.7 Histochemical detection of β-galactosidase expression in organs of lacZ reporter CTSO mice

All animal care and use procedures were performed in accordance with the European Community Standards on the Care and Use of Laboratory Animals (Directive 2010/63/EU) Mice were maintained at the accredited animal care facility 'Unité de thérapeutique Experimentale (UTE, accreditation number C44-015 by the French Ministry of Agriculture).

Visualization of β-galactosidase expression was done in dissected organs from 6-month old control and heterogous LacZ-reporter CTSO C57BL/6 mice ($Ctso^{tm2b(KOMP)Wtsi}$ (MGI:5637109; Charles River). Mice were euthanized by intraperitoneal injection of sodium pentobarbital (100 µL Euthasol Vet, Dechra) in compliance with institutional guidelines. After confirmation of death, animals were perfused transcardially with 25 mL ice cold phosphate-buffered solution (PBS) containing heparin, followed by 20 mL freshly prepared 4 % paraformaldehyde (PFA; Sigma–Aldrich). The brain and the abdominal aorta were dissected and post-fixed for 30 min at 4°C in 1% PFA supplemented with 0.05% glutaraldehyde (Sigma–Aldrich). After two washes in PBS, β-galactosidase activity was detected using the gals-1kt X Gal staining kit (Sigma–Aldrich) with 24 h incubation at 37°C, followed by PBS washes and imaging under a stereomicroscope. Samples were cryoprotected sequentially in 15% and 30% sucrose solutions during 24 h each, embedded in OCT compound (Tissue Tek), rapidly frozen in isopentane at −80°C, and stored until sectioning. For the aorta, serial 10 µm sections were cut on a NX70 cryostat (Thermo Scientific) and mounted on glass slides for observation.

2.8 Cell isolation and culture

Primary VSMC were isolated from arteries of 4-week-old male Wistar–Kyoto (WKY) rats. Rats were sacrificed by decapitation after isoflurane (4%) inhalation according to institutional animal handling ethics. For isolation of aortic VSMC, the aorta was harvested, cleaned, endothelium-denuded, cut into small pieces and digested by collagenase II (1 mg/mL; 2 h at 37°C under agitation; Worthington Biochemical). After inactivation of collagenase with serum, the tissue was spun down and plated in a 6-well plate in Dulbecco modified Eagle medium (DMEM, Gibco; Invitrogen) containing 10% foetal bovine serum (FBS), 4.5 g/L glucose, 100 units/mL penicillin, and 100 µg/mL streptomycin at 37°C-5% CO_2. Subcultures of these cells were obtained by trypsinization using a solution of porcine trypsin (0.05%) in Ca^{2+}–Mg^{2+}-free PBS with EDTA (0.02%).

For isolation of cerebral artery VSMC, the circle of Willis was dissected under a stereomicroscope and placed in ice-cold PBS containing 1% penicillin–streptomycin. The arteries were then carefully cleaned, rinsed, and centrifuged at 300×*g* for 5 min. Arterial segments were digested by collagenase type II (Worthington Biochemical Corporation, 1 mg/mL in DMEM containing 1% penicillin–streptomycin, 1/1000 amphotericin B) for 45 min at 37°C under agitation. The digestion was stopped by adding DMEM supplemented with 20% FBS, 1% penicillin–streptomycin, and 1/1000 amphotericin B. After centrifugation (300 ×*g*; 5 min) and discarding of supernatant, the pellet was washed and centrifuged twice in 10 mL of complete DMEM under same conditions before being plated into 12-well culture plates pre-coated with 0.1% gelatin and filled with 1 mL of complete DMEM (20% FBS). From day 3 after seeding, cell migration was checked and DMEM was regularly replaced until passaging. The cells were passaged when cell density reached 80–90% using accutase solution (Invitrogen) with trypsin (0.01%) in Ca^{2+}–Mg^{2+}-free PBS with EDTA (0.02%) for 5 min at 37°C, and reseeded on 0.1% gelatin-coated plates. All experiments in VSMC were performed between passages 2 and 4. When indicated, VSMC were seeded onto culture plates pre-coated with FN (F2006, Sigma–Aldrich, 20 µg/mL). For cell stretching, cyclic uniaxial strain was applied at 1 Hz and 10% or 20% strain for 24 h (MechanoCulture FX, CellScale). NIH3T3 cells were cultured in DMEM containing 1 g/L glucose, 10% FBS, 100 units/mL penicillin and 100 µg/mL streptomycin at 37°C-5% CO_2.

2.9 RT–qPCR

Total RNA was purified from cells, using RNA plus kit (Macherey Nagel), and from rat cerebral arteries using TRIzol reagent (MAN0001271, Ambion, Thermo Fisher Scientific) and RNA XS Plus kit (Macherey Nagel) according to the manufacturer instructions. Cerebral arteries from 3-months-old WKY, spontaneously hypertensive (SHR), and stroke-prone SHR (SPSHR) male rats (300 g) have been previously collected and snap-frozen in liquid nitrogen before RNA extraction. RNA (500 ng) was reverse-transcribed with M-MLV enzyme (28025021, Thermo Fisher Scientific). Real-time qPCR was performed on a 7900HT Fast Real-Time PCR System (Applied Biosystems) using SYBR Green Master Mix (4367659, Applied Biosystems) and primers listed in Supplementary material online, *Table S4*. Each sample was analysed in triplicate. GAPDH was used as the reference gene and results are expressed according to the $2^{-\Delta\Delta Ct}$ method.

2.10 Immunoblotting

Supernatant from VSMC or NIH3T3 were taken off and concentrated with Amicon Ultra-0.5 Centrifugal Filter Unit (UFC5010, Millipore). Cells were lysed on ice in buffer supplemented with protease and phosphatase inhibitor cocktails (Sigma–Aldrich) and sodium orthovanadate. Equal amount of proteins of each sample was separated by SDS-PAGE, transferred to nitrocellulose membranes, and incubated with specific antibodies: CTSO (for rat: ab200735, Abcam, for human: HPA002041, Sigma–Aldrich), CTSB (sc-36558, Santa Cruz Biotechnology), CTSK (sc-48353, Santa Cruz Biotechnology), CTSS (sc-74429, Santa Cruz Biotechnology), cleaved caspase 3 (9664, Cell Signalling Technology), P-FAK (8556, Cell Signalling Technology), FAK (3285, Cell Signalling Technology), FN (15613-1-AP, Proteintech), type I collagen (14695-1-AP, Proteintech). Equal loading was checked by reprobing of the membrane with an anti-tubulin antibody (T9026, Sigma). Immune complexes were detected with appropriate secondary antibodies and enhanced chemiluminescence reagent (Clarity ECL BioRad). Protein band intensities were quantified using ImageJ Software (NIH software, Bethesda, Md).

2.11 *CTSO* silencing

VSMC were transfected using Lipofectamine RNAiMAX reagent (Invitrogen) according to the manufacturer instructions with a pool of siRNAs targeting rat *Ctso* (ON-TARGETplus siRNA-SMARTpool) (Cat# L-110260-00-0005; Horizon Discovery) and a non-targeting control pool (Pool #1, D-001810-10-05, Horizon Discovery) to generate KD-SMC and Cont-SMC, respectively. The efficiency of *Ctso* mRNA depletion was assessed 72 h post-transfection by RT–qPCR.

2.12 Viability/proliferation assay

VSMC viability/proliferation was quantified by MTT (3-[4,5-dimethylthiazol-2-yl]-2,5-diphenyltetrazodium) colorimetric assay according to the manufacturer instructions (M5655; Sigma–Aldrich). Briefly, VSMC were seeded onto 96-well plates in triplicate for each condition, cultured for 24 h, after which they were serum-starved for 24 h. VSMC were then incubated in DMEM without or with 10% FBS for 24 h. The number of viable cells was then determined by incubation in 1 mg/mL MTT for 4 h at 37°C. The medium was then removed and acidified isopropanol was added to solubilize the MTT reduction product formazan. MTT reduction by viable cells was then quantified by measurement of the absorbance at 590 nm.

2.13 Apoptosis assay

VSMC apoptosis was determined after incubation in 1 µmol/L staurosporine (S5921, Sigma–Aldrich) in serum-free medium for 8 h. Apoptosis was quantified by the measurement of cleaved caspase 3 by western blot and by TUNEL assay. VSMC were fixed with 4% paraformaldehyde

and permeabilized. Fragmented DNA was stained with TUNEL Assay Kit-BrdU-Red (ab66110, Abcam) according to manufacturer instructions, and DAPI was used to label all nuclei. Coverslips were mounted on slides with Prolong gold antifade reagent and observed with a fluorescent microscope. Apoptotic cell number was quantified as the percentage of TUNEL-positive cells.

2.14 Transwell migration assay

Boyden chamber assay was performed as previously described.[21] VSMC, transfected with siRNA 48 h before, were trypsinized and washed in serum-free DMEM before plating into transwells (0.47 cm^2 of culture area, 8 µm pore size; Nunc™). DMEM containing 10% FCS was placed in the lower chamber and VSMC were allowed to migrate for 10 h at 37°C. After incubation, the filter was removed and VSMC on the upper side of the filter were scraped off. VSMC that had migrated to the lower side of the filter were fixed with 4% paraformaldehyde and stained with Coomassie blue 0.1% for observation under a microscope in brightfield mode. Migration to the lower chamber of the transwell was quantified by the area covered by cells measured using ImageJ Software and expressed expressed relative to Cont-SMC set as 1.

2.15 Cell adhesion assay using impedance technology

VSMC (10 000/well) were seeded in a 96 well plate microtiter xCELLigence assay plate coated with 2 µg/mL FN (E-Plate, ACEA Biosciences Inc.) and placed on the Real-time xCELLigence Cell Analyzer (Roche Applied Science) platform at 37°C. The cell index value, which are proportionate to the area covered by the cells was measured every 5 min for a period of 8 h. Adhesion speed was defined as the slope of the cell index change over time.

2.16 Collagen gel contraction assay

VSMC were mixed with collagen gel working solution (CBA-201, Cell Biolabs). The cell-collagen mixture was added into a 24-well plate and incubated at 37°C for 1 h to allow collagen polymerization. Serum-free DMEM was added to the top of the collagen gel lattice. After 24 h, cells were treated or not with U46619 (10^{-6} mol/L) and the myosin inhibitor BDM (from CBA-201 kit), and the collagen gels were released by a sterile spatula. Changes in the collagen gel area were measured at 48 h. The percentage of contraction corresponded to [(area in BDM condition-area in the control or U46619 condition)/area in BDM condition × 100].

2.17 Immunofluorescence

VSMC were seeded onto culture plates pre-coated with human FN (F2006, Sigma–Aldrich, 20 µg/mL). After 24-h of culture, cells were fixed with 4% paraformaldehyde for 15 min, rinsed twice with PBS, then permeabilized and blocked for 1 h with carbonate–bicarbonate buffer containing 1% FBS, 3% BSA, 0.5% Triton X-100, 0.01% deoxycholate, 0.02% sodium azide. FN was stained with anti-human FN antibody (F3648, Sigma–Aldrich; 1/500 overnight), revealed by a secondary Alexa647-conjugated donkey anti-rabbit antibody (LifeTech; 1/1000, 2 h). Actin staining was performed at room temperature using phalloidin Alexa Fluor™ 488 (A12379, Fisher Scientific; 1/400, 45 min). Images were taken using Nikon A1 confocal microscope (Nikon France, Champigny sur Marne) equipped with a ×60 Plan-Apochromat objective with a numerical Aperture of 1.4. FN fluorescence was quantified using FIJI. Briefly, for each cell a mask corresponding to the cell area was generated and applied on the FN staining image. FN fluorescence intensity in this area was extracted for each cell.

2.18 Atomic force microscopy experiments

Atomic force microscopy (AFM) experiments have been performed in Cont- and KD-SMC grown on plastic and allowed to produce their own ECM for 5 days. ECM analysis has been performed after decellularization as previously described.[22] All experiments were then performed in Physiological Saline Solutions buffered with 20 mM HEPES at 37°C using a NanoWizard® atomic force microscope (JPK Instruments, Germany) equipped with a temperature controller and inverted optical microscope. Indentation experiments were carried out with cantilevers (SQube) having a colloidal glass sphere of 5 µm in diameter. Their spring constant was calibrated using the thermal noise method implemented in the AFM setting (JPK software), with values comprised between 0.12 and 0.15 N m^{-1}. Prior to indentation measurements, the cantilever sensitivity was systematically measured from the slope of force–distance curves performed on glass. The optical microscope was first used to position the AFM tip on ECM or on the cytoplasmic region of the selected cell and several approach-retract force–distance curves were performed to determine the force to be applied corresponding to an indentation depth of ∼500 nm (a good compromise avoiding the long-range interactions and in the validity domain of the Hertz contact mechanics model). Then, force–distance curves were recorded on cells at a low constant speed of 1 µm/s to neglect the hydrodynamic drag forces exerted on the cantilever by the liquid medium.[23] These curves were then converted into force-indentation curves, and the approach part was fitted by the Hertz model to determine the apparent elastic modulus of cells.[24]

2.19 Surface plasmon resonance studies

Surface plasmon resonance (SPR) was used to assess the interaction between FN (ECM001, Sigma–Aldrich), with CTSO (MBS717933; Clinisciences) immobilized onto CM5 (1000 RU; GE Healthcare) using a Biacore T200 (GE Healthcare). Single-cycle kinetics was performed by 2 min-sequential injections at a flow rate of 40 µL/min of five increasing concentrations of CTSO (12.5; 25; 50; 100 and 200 nM) over the FN-functionalized substrate (ECM001, Sigma–Aldrich). CTSO sensorgram was corrected by subtracting a sensorgram obtained from a reference flow cell with no immobilized protein. Global fitting of the data to a Langmuir 1:1 model was used to determine the association (k_a), dissociation (k_d), and the affinity constant (K_D) with T200 Biaevaluation Software (Biacore). K_D values for CTSO and FN were determined using the steady-state method.

2.20 Mutagenesis

CTSO-TurboGFPpPlasmid was purchased from Origene (RG208268). c.128C > T *CTSO* and c.946G > A *CTSO* mutagenesis was performed using Q5® Site-Directed Mutagenesis Kit Protocol (E0554, NEB) and designed primers: A43V-Fw: 5′-GAAGCCGCCGTCTTCCGGGAAAGTC-3′; A43V-Rv: 5′-ACG CTCGCGGCTCCGCGG-3′; V316I-Fw: 5′-GTTTGT GGTATTGCAGATTCCATTTCTTCTATATTTGTGACGC-3′; V316I-Rv: 5′-GCGTCACAAATATAGAAGAAATGGAATC TGCAATACCAC AAAC-3′. Mutations were confirmed by standard sequencing methods using T7 standard primer and designed primer (5′-AAGCCCCTGGAA GACCTAAG-3′).

2.21 Generation of lentiviral constructs

LT3GEPIR plasmid (#111177, Addgene) was modified to remove miR30 backbone by amplifying and cloning eGFP between XhoI and EcoRI restriction sites using the following primers: Fw 5′-CGGCCGCTCGAGAT GGTGAGCAAGGGCGAGGAG-3′ and Rv 5′-GATCTGAAT TCTTA CTTGTACAGCTCGTCCATGC-3′. The resulting plasmid was used to clone WT and mutant CTSO in BamHI and XhoI,

2.22 Lentivirus production, transduction, and induction of WT-CTSO and CTSO variants

Lentiviral vector for expressing WT-CTSO, p.Ala43Val-CTSO and p.Val316Ile-CTSO was transfected into HEK293T cells along with packaging vectors psPAX2 and pVSVG2 (provided by Dr. Utz Fischer's lab)

using polyethylenimine (#764965, Sigma–Aldrich) transfection agent. After overnight incubation, the medium was replaced with fresh medium (DMEM + 10% serum). Forty-eight hours and 72 h after transfection, viral supernatant was collected, filtered through 0.22 µm filter and used to infect NIH3T3 in the presence of polybrene (8 µg/mL, H9268; Sigma–Aldrich). After 48 to 72 h of infection, transduced NIH3T3 cells were selected with puromycin (2 µg/mL, P8833, Sigma–Aldrich) for 48 h and maintained in the presence of puromycin (2 µg/mL). The induction of WT- or mutated CTSO was performed at least 2 days before the experiment by supplementing the medium with doxycycline (1 µg/mL, #D9891, Sigma–Aldrich), which was maintained until the completion of the experimental procedure.

2.23 Statistical analysis

Data are expressed as the mean ± SEM of sample size *n*. All values use biological replicates and are indicated by group size *n* in figure legends or within graphs. For *in vivo* data, each *n* value corresponds to a single animal. For *in vitro* data, each *n* value corresponds to an independent experiment. Investigators were blinded for some measurements made (i.e. immunofluorescence, immunohistology, area measurement). Comparisons between two groups were performed by two tailed non-parametric Mann–Whitney *U* test, and ANOVA with relevant *post hoc* tests was used for multiple-group comparisons using GraphPad Prism 6.0 software (GraphPad Software). $P < 0.05$ was considered statistically significant.

3. Results

3.1 Identification of one rare coding variant affecting *CTSO* in a familial case of IA

We first recruited a large family (*Figure 1A*) with six definite carriers of IA in two generations, among whom two had a history of IA rupture. In this family, there were also four relatives with suspected IA (I:1, II:3, and II:4 because of unexplained sudden death; III:14 with a doubtful ectasia on MRI, see Supplementary material online, *Figure S1A*), three individuals with unknown phenotypes in the absence of MRI screening, and 19 subjects without IA detected on MRI. Among the definite carriers of IA, all were females and three were carriers of multiple IA (with a maximum of four IAs detected for subject II-9). Of the 12 IAs detected in the family, six were located in the MCA territory (50%), three in the ACA (25%), two in the PCA (16%), and one in the ICA territory (9%) (*Figure 1B* and *C*). The median maximal diameter of IA was 4 mm (min 3 mm, max 8 mm). We applied WES to three affected members of the family (II9, III2, III4; *Figure 1A*). Out of the 77 to 107 rare non-synonymous or splicing variants detected in each three whole exomes, we found that only eight were shared between the three affected relatives (see Supplementary material online, *Tables S1* and *S2*). IBD analysis on all available relatives revealed that only one of the eight variants resides within a shared haplotype—located at 4q32—between the six affected subjects (see Supplementary material online, *Tables S1* and *S3*). We then confirmed this finding by capillary sequencing. This missense variant in the *CTSO* gene, *CTSO* c.946G > A

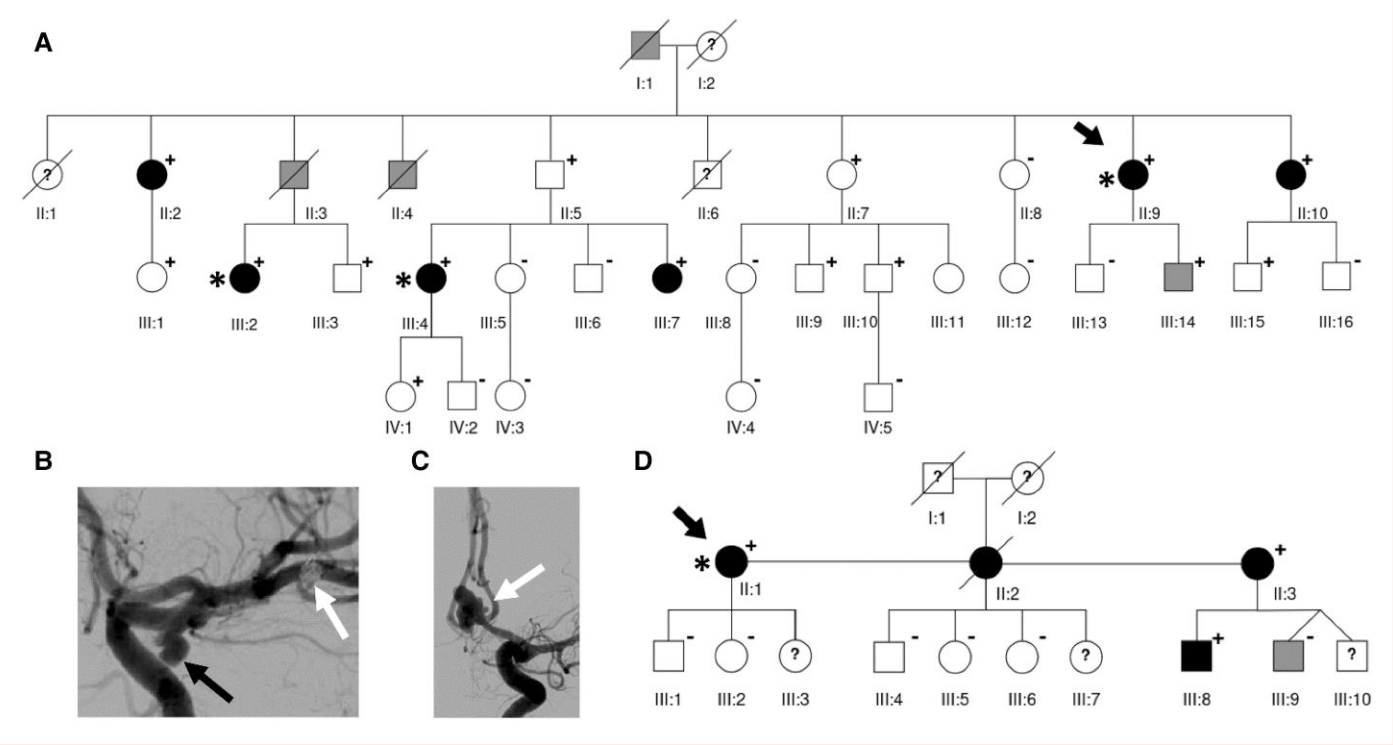

Figure 1 Genetic investigations in families with multiple IA-affected case subjects. (*A*) Pedigrees of family A showing the segregation pattern of the rare functional variant c.946G > A in *CTSO*. Black boxes, empty boxes, grey boxes, and boxes with question marks indicate IA-affected case subjects, non-affected relatives, and individuals with uncertain and unknown status, respectively. Plus/minus signs indicate the presence/absence of the *CTSO* variant. Arrows indicate the index case subject in each family, while asterisks indicate the individuals included in WES analysis. (*B*) Digital subtracted angiography showing two IA carried by the index case II-9 of family A: one located on the middle cerebral artery and already treated by coiling (white arrow), and one located on the posterior communicating artery (black arrow). (*C*) Digital subtracted angiography showing one ruptured IA just before treatment, located on the anterior communicating artery of the case III-4 of family A (white arrow). (*D*) Pedigrees of family B showing the segregation pattern of the rare functional variant c.128C > T in *CTSO*.

Table 1 Rare functional variants in *CTSO* shared by all IA-affected subjects in families A and B

Family	Genomic position (GRCh37/hg19)	Gene	Nucleotide consequence	Protein consequence	MAF in NFE[a] (gnomAD v4.1)	Predicted functional impact		Cases/Total	
						SIFT	Polyphen 2	Affected	Unaffected
A	4:156847208	*CTSO*	c.946G > A	p.Val316Ile	1.7×10^{-5}	Deleterious	Probably damaging	6/6 (6F, 0 M)	8/19 (3F, 5 M)/(10F, 9 M)
B	4:156874872	*CTSO*	c.128C > T	p.Ala43Val	6.5×10^{-4}	Tolerated	Probably damaging	3/3 (2F, 1 M)	0/5 (2F, 3 M)

Mutation names are based on Ensembl *CTSO* transcript ENST00000433477.3.
The number of affected and non-affected females (F) and males (M) is indicated.
MAF, Minor Allele Frequency; NFE, non-Finnish Europeans; GnomAD, genome Aggregation Database; GERP, Genomic Evolutionary Rate Profiling; SIFT, Sorting Intolerant from Tolerant.
[a]$n = 590\,031$ individuals (556 006 whole exomes and 34 025 whole genomes).

Table 2 Clinical characteristics, treatments, and exposition to risk factors for IA cases and unaffected relatives according to CTSO status

	CTSO variants IA	*CTSO* variants no IA	No *CTSO* variant no IA	*P*-value
n	9	8	16	–
Age (yr) [median (range)]	69 (51–93)	60 (38–89)	49 (33–76)	–
Female	8 (88.9%)	3 (37.5%)	9 (56.3%)	0.088
Smoker or former smoker	4 (44.4%)	5 (62.5%)	8 (50%)	0.816
Alcohol intake >150 g per week	4 (44.4%)	1 (12.5%)	3 (18.8%)	0.326
High blood pressure	5 (55.6%)	2 (25%)	1 (6.3%)	0.013
Dyslipemia or diabetes	2 (22.2%)	2 (25%)	0 (0%)	0.080
Anti-platelet treatment	2 (22.2%)	1 (12.5%)	1 (6.3%)	0.666
Anti-inflammatory drugs	0 (0%)	0 (0%)	1 (6.3%)	1.000
Statin treatment	1 (11.1%)	1 (12.5%)	1 (6.3%)	1.000
Oral anticoagulant treatment	1 (11.1%)	2 (25%)	4 (25%)	0.745

Data are expressed as median (minimum and maximum) for age and as count (and percentage) for all other categorical variables. The Fisher exact probability test was used for contingency comparison between groups.

(p.Val316Ile), is found with a MAF of 1.7×10^{-5} among the NFE population in gnomAD v4.1, reported with a Genomic Evolutionary Rate Profiling (GERP) score of 5.68 and predicted in silico as damaging for CTSO protein structure and function by both PolyPhen-2 and SIFT (*Table 1*).

3.2 A second familial case of IA associated with rare *CTSO* coding variant

To further investigate the putative involvement of *CTSO* in IA susceptibility, we then screened for rare functional variants within this gene among 93 additional index cases with familial forms of IA, for which WES data were available in-house. We found one additional rare missense variant, *CTSO* c.128C > T (p.Ala43Val), in one case (*Table 1*). The corresponding family (*Figure 1D*) comprised four IA carriers (three females and one male), among whom one carried two IAs. The median maximal diameter of IA was 5 mm (min 4 mm, max 9 mm). Three IAs were located in the MCA territory, one in the ACA and one in the ICA territory, while in one case the location was undetermined. By capillary sequencing, we tested the *CTSO* c.128C > T variant among family members and detected it in the three tested IA carriers but in none of their six non-affected relatives (including the subject III-9 with uncertain phenotype, Supplementary material online, *Figure S1B*). This variant, found with a MAF of 6.5×10^{-4} among the NFE population in gnomAD v4.1 and reported with a GERP score of 3.67, was predicted in silico as damaging by PolyPhen-2 but not by SIFT (*Table 1*).

3.3 Clinical characteristics and exposition to risk factors according to *CTSO* status

When comparing subgroups of individuals with or without *CTSO* variant and carrying or not IA among the two families members, we observed a higher proportion of subjects with history of high blood pressure among the IA carriers ($P = 0.013$) while we found no significant differences regarding age, proportion of women, smoking habits, history of ischaemic stroke, level of alcohol consumption, history of diabetes or dyslipidaemia, treatment with statin, anti-platelet, oral anticoagulant, and anti-inflammatory medication (*Table 2*).

3.4 CTSO is expressed in cerebral arteries

To explore the putative implication of CTSO in IA pathophysiology, we first sought to investigate the expression of CTSO in cerebral arteries. *Ctso* mRNA was found at a similar level in cerebral arteries of WKY rats and in arteries from SHR and SPSHR, suggesting that *Ctso* mRNA was expressed in cerebral arteries but was not modulated by high blood pressure (*Figure 2A*). To characterize CTSO expression more precisely, we used mice expressing the *LacZ* gene as a reporter gene to document CTSO expression in arterial walls. X-gal staining of the whole brain clearly showed a blue signal in the arteries of the circle of Willis (*Figure 2B*). In the aorta, examination of cross sections revealed a strong β-galactosidase activity in the media layer indicating expression in VSMC, while no staining was observed in the intimal layer (*Figure 2C*). In summary, as indicated by β-galactosidase activity, CTSO is expressed in the arterial

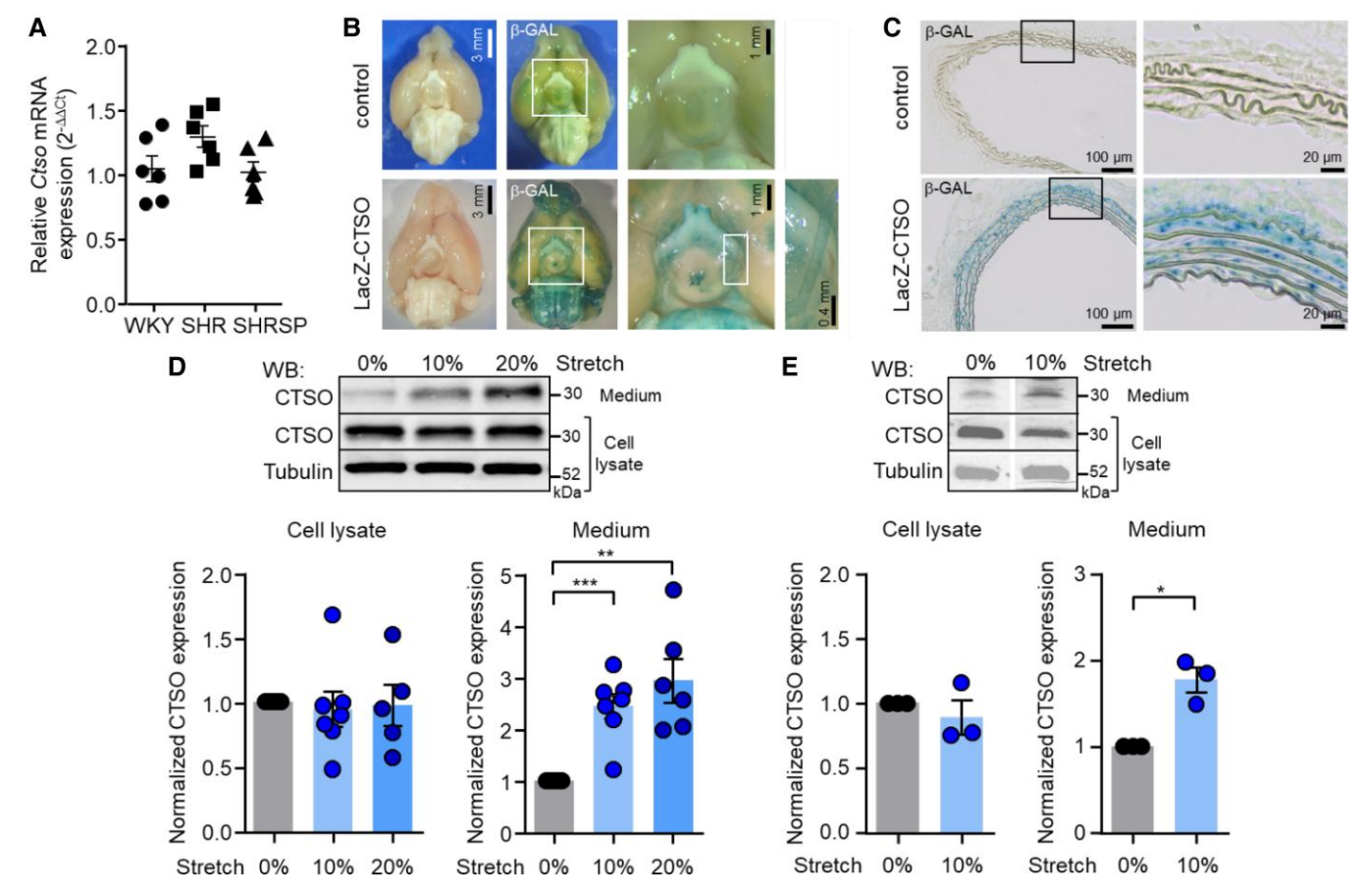

Figure 2 CTSO expression in arteries and arterial smooth muscle cells. (*A*) *Ctso* mRNA expression analyzed by quantitative RT–PCR in cerebral arteries of normotensive (WKY), and hypertensive rats (SHR and SHRSP) ($n = 6$ biological replicates; results were expressed relative WKY and presented as mean ± SEM; *ns*, Kruskal–Wallis test). (*B*) Detection of β-gal activity in the brain of control and lacZ reporter mice for CTSO reporter mice via X-gal staining (blue). The white squares outline the enlarged area of the image displayed next to it showing expression in the cerebral arteries of the circle of Willis. (*C*) Cross sections of X-gal stained aorta of lacZ reporter mice for CTSO reporter mice. The black squares outline the enlarged area of the image displayed next to it showing blue staining in the media. (*D*) Representative western blots and quantification of CTSO protein expression assessed in cell lysate and culture medium of aortic VSMC cultured in static condition and subjected to 10 and 20% cyclic stretch. Tubulin was also blotted to check equal loading in cell lysate ($n = 5$–7 biological replicates). (*E*) Representative western blots and quantification of CTSO protein expression assessed in cell lysate and culture medium of cerebral artery VSMC cultured in static condition and subjected to 10% cyclic stretch. Tubulin was also blotted to check equal loading in cell lysate ($n = 3$ biological replicates). (Data are expressed as mean ± SEM; *$P < 0.05$, **$P < 0.01$, and ***$P < 0.001$; one-sample *t* test.)

walls, including in the cerebral arteries of the circle of Willis, particularly in the media layer. Analysis in primary cultures confirmed the expression of CTSO in VSMC isolated from aorta (*Figure 2D*) and cerebral arteries (*Figure 2E*). CTSO was found in VSMC lysates but also in the culture medium, indicating the secretion of the protein (*Figure 2D* and *E*). Moreover, CTSO secretion was potentiated by stretch, without any change in mRNA level (*Figure 2D, 2E* and Supplementary material online, *Figure S2*). Interestingly, CTSO is expressed in the arterial wall of human IA domes (*Figure 3A*). In unruptured IA, CTSO seemed to be minimally expressed in few cells, but no CTSO staining was observed in the ECM. A significantly higher content of CTSO, particularly in the ECM, was detected in the arterial wall of ruptured IA thus confirming the CTSO secretion in the extracellular space by VSMC observed *in vitro*, particularly under stretching condition (*Figure 3B*).

3.5 *CTSO* silencing does not affect VSMC proliferation and apoptosis

We next aimed to elucidate the role of CTSO in the arterial wall by focusing on VSMC, in which its secretion is modulated by stretch. To this end, we evaluated the consequences of siRNA-mediated knockdown of endogenous CTSO in VSMC (KD-SMC) in comparison with a control siRNA pool (Cont-SMC). In KD-SMC, CTSO protein expression was reduced by 60 and 80% in aortic and cerebral artery VSMC, respectively, without any effect on other members of the cathepsin family (CTSB, CTSS, CTSK; Supplementary material online, *Figure S3*). *Ctso* silencing did not affect VSMC proliferation (*Figure 4A*), nor apoptosis as measured by TUNEL and caspase 3 cleavage in basal condition (no apoptosis, data not shown) and after induction of apoptosis by staurosporine (*Figure 4B* and *C*). These results indicate that CTSO did not affect VSMC proliferation and viability.

3.6 *CTSO* silencing modifies VSMC migration and adhesion

We next tested whether CTSO regulates the migratory and adhesive properties of VSMC using Boyden chambers and adhesion assays, respectively. CTSO depletion in VSMC led to a significant decrease in transmigration (*Figure 4D*). Adhesion speed of VSMC on plastic or on collagen coating

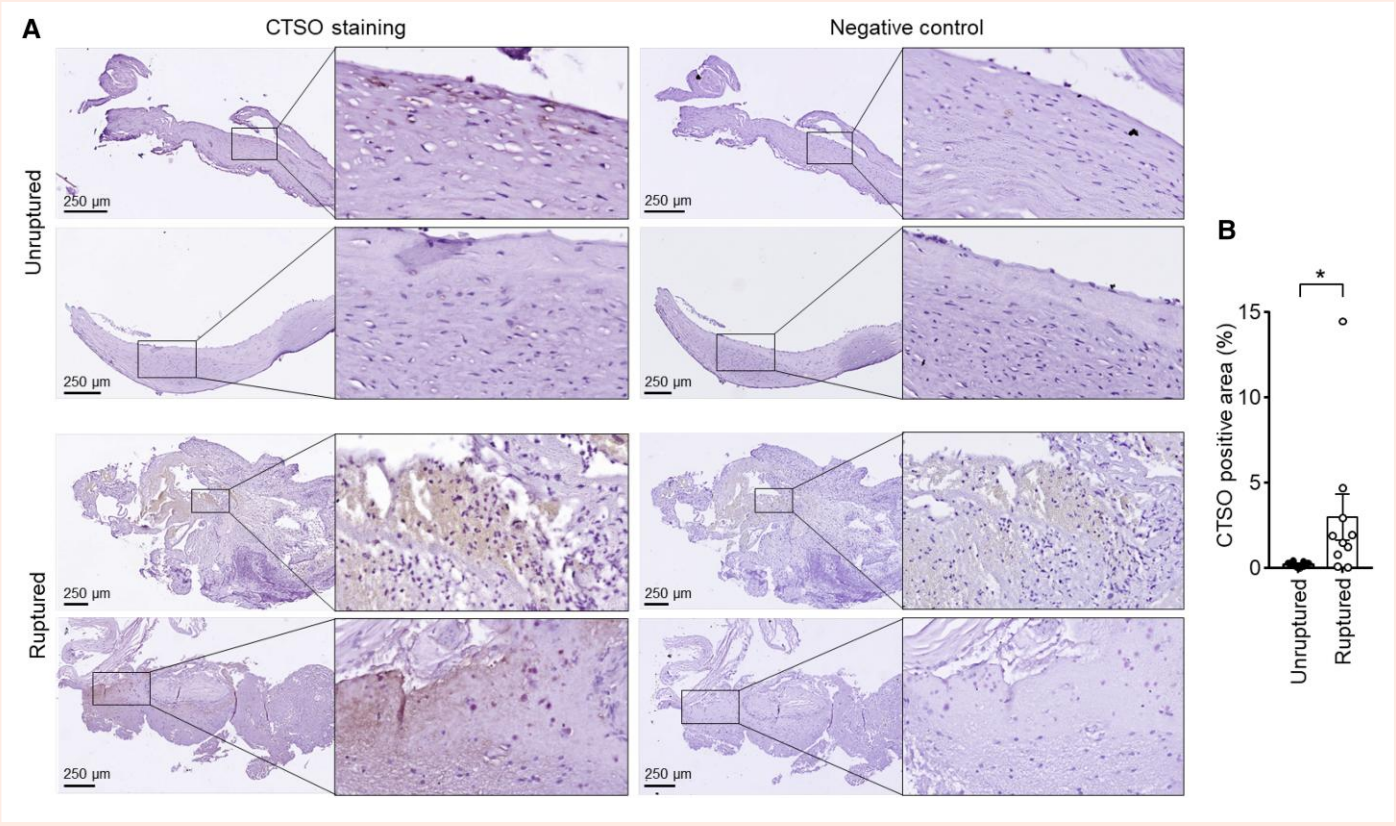

Figure 3 Expression of CTSO in human IA domes. (*A* and *B*) Representative whole images of immunochemical staining of CTSO (in brown) and their respective negative controls (*A*) and quantification of CTSO positive area (*B*) in human unruptured ($n = 10$ biological samples) and ruptured IA domes ($n = 10$ biological samples). The black rectangles represent the region shown at higher magnification on the right side of each image. (Results were expressed as mean ± SEM; $*P < 0.05$; Mann–Whitney test.)

was not significantly affected by CTSO depletion (see Supplementary material online, *Figure S4A* and *B*). However, knocking-down *CTSO* accelerated the adhesion speed of VSMC from aorta (*Figure 4E*) and cerebral arteries (*Figure 4F*) on FN matrix. This increased speed of adhesion in KD-SMC on FN was reversed by the addition of exogenous CTSO in the culture medium (*Figure 4F*). The observed accelerated adhesion in KD-SMC was associated with an increased phosphorylation of focal adhesion kinase (FAK) in KD-SMC compared to Cont-SMC, both at 2 and 24 h after seeding on FN matrix (*Figure 5A*). When VSMC were plated on plastic, without FN coating, a significant increase in FAK phosphorylation was also observed at 24 h in KD-SMC compared to Cont-SMC, but not at 2 h post-seeding (*Figure 5B*). In contrast, when VSMC grew on collagen matrix, FAK phosphorylation remained similar in KD-SMC and Cont-SMC at 2 and 24 h (see Supplementary material online, *Figure S4C*). It is known that VSMC produce and release FN which, in turn, can modulate their phenotype and functions.[25] The observed differences in FAK phosphorylation induced by CTSO depletion may therefore results from an effect on the endogenous FN. To test this hypothesis, we thus analysed the effect of *CTSO* silencing on FN expression in Cont- and KD-SMC cultures. Western blot analysis revealed an increased level of FN in KD-SMC compared to Cont-SMC, while there was no difference in collagen I (COL-I) expression (*Figure 5C*). This rise in FN expression in KD-SMC was not associated with a change in mRNA-*Fn1* level which, like mRNA-*Col1a*, remains the same in Cont- and KD-SMC (*Figure 5D*). The observed increase in FN level induced by CTSO silencing could therefore stem from the ability of CTSO to degrade FN. To test this hypothesis, we cultured Cont- and KD-SMC on human FN, which we quantified by immunofluorescent labelling. FN labelling confirmed the presence of a greater amount of FN in the vicinity of KD-SMC compared to Cont-SMC (*Figure 5E*). All together, these data show that CTSO controls VSMC migration and adhesion, and suggest that it could result from an effect on FN. We thus used surface plasmon resonance (SPR) to determine whether there is a direct interaction between CTSO and FN. Sensorgram of CTSO clearly exhibited typical binding response (*Figure 5F*). The analysis of the association of CTSO with FN by using a global 1:1 Langmuir model of interaction revealed an equilibrium dissociation constant (K_D) value of 1 nM (*Figure 5F*). Binding of CTSO with FN is characterized by an association rate constant $[k_a] = 8.84 \times 10^4\ m^{-1}\ s^{-1}$ and a dissociation rate constant of $[k_d] = 8.85 \times 10^{-5}\ s^{-1}$), thus revealing that CTSO directly interacts with FN with a high affinity.

3.7 *CTSO* silencing affects contractile phenotype marker gene expression

We next assessed the potential role of CTSO on VSMC phenotype by measuring the expression of contractile marker gene expression (*Figure 6A*). Compared with Cont-SMC, the expression of all tested VSMC marker mRNAs, namely *Acta2*, *Myh11*, *Tagln*, and *Cnn1* was significantly up-regulated in KD-SMC, which showed a 90%-decrease in *Ctso* mRNA expression (*Figure 6B*). By contrast, the expression of *Bmp4*, a known marker of osteogenic differentiation of VSMC[26] was reduced in KD-SMC compared to Cont-SMC (*Figure 6B*). These results suggest that *Ctso* silencing reinforced VSMC contractile phenotype. However, measurement of contractility showed that KD-SMC contracted collagen gel less strongly than Cont-SMC in response to the thromboxane A2 analog U46619 (*Figure 6C*).

3.8 *CTSO* silencing induces stiffening of VSMC

We then used AFM to assess the effect of CTSO depletion on VSMC and VSMC-derived ECM stiffness, as arterial stiffening is known to be a risk

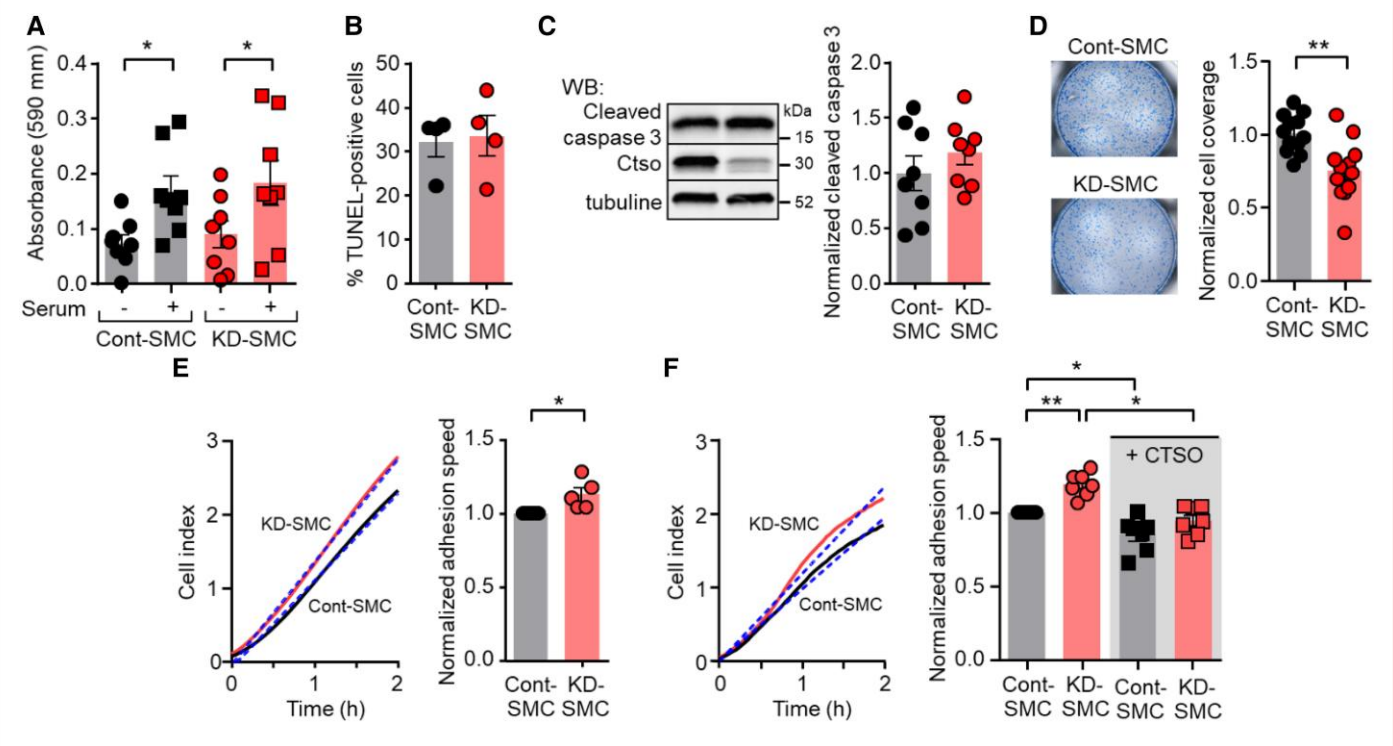

Figure 4 Consequence of CTSO depletion on VSMC proliferation, apoptosis, migration, and adhesion. (*A*) Proliferation assessed by the measurement of MTT absorbance in the absence and presence of 10% serum in aortic VSMC transfected with siRNA targeting *Ctso* (KD-SMC) and control siRNA (Cont-SMC) ($n = 8$ biological replicates). (*B*) Number of apoptic aortic cells in KD-SMC and Cont-SMC culture after stimulation with staurospaurine (1 µmol/L, 8 h). Values represent the percentage of TUNEL-positive cells relative to total cell population in each group ($n = 4$ biological replicates). (*C*) Typical Western blot of cleaved-caspase 3 in Cont- and KD-SMC (aortic) and corresponding quantification. CTSO and tubulin have been also blotted to check CTSO silencing and equal loading ($n = 8$ biological replicates). (*D*) Representative images of Cont- and KD-SMC (aortic) which migrated to the underside surface of transwell membranes and the corresponding quantification ($n = 12$ biological replicates). (*E* and *F*) Representative curve showing the cell index representing the adhesion of Cont- and KD-SMC from aorta (*E*) and cerebral artery (*F*) over time and quantification of the adhesion speed on FN-coated plates ($n = 5$ (*E*) and $n = 7$ (*F*) biological replicates). The effect of addition of recombinant CTSO (200 ng/mL) on the adhesion speed of cerebral artery SMC is also shown in *F*. (Results were expressed relative to Cont-SMC set as 1 (except in *B*). Data are presented as mean ± SEM; $*P < 0.05$, $**P < 0.01$; one-way *ANOVA* with Holm–Sidak post hoc test in A; Mann–Whitney test in (*B–D*); One-sample *t* test in *E* and *F*).

factor for IA.[27] Elastic modulus determined by AFM nanoindentation showed that the stiffness of KD-SMC was significantly higher than that of Cont-SMC, and was strongly reduced by complementation with exogenous CTSO (*Figure 7A* and Supplementary material online, *Figure S2*). In contrast, the corresponding ECM produced by KD- and Cont-SMC displayed a similar stiffness (*Figure 7A* and Supplementary material online, *Figure S5*).

3.9 CTSO variants

To assess the impact of c.128C > T *CTSO* and c.946G > A *CTSO* variants on CTSO protein we established stable cell lines expressing wild-type (WT-CSTO), and the two mutated proteins, p.Val316Ile-CTSO and p.Ala43Val-CTSO. Western blot analysis showed that expression level in cell lysates was similar for WT-CTSO and the two mutated CTSO proteins (*Figure 7B*). In contrast, the amount of p.Val316Ile-CTSO and p.Ala43Val-CTSO in the culture medium was strongly reduced compared to WT-CTSO (*Figure 7B*). Since we observed an increase in the amount of FN after CTSO depletion in VSMC (*Figure 5C*), we investigated the effect of p.Val316Ile-CTSO and p.Ala43Val-CTSO expression on FN level. Western blot results show that the expression of CTSO mutants mimicked the effect of CTSO depletion on the increase of FN level, without affecting COL-I expression (*Figure 7C*).

4. Discussion

We have identified two rare missense variants in the *CTSO* gene shared by all the affected relatives in two large pedigrees with multiple IA-affected relative. Of note, we also observed several subjects ($n = 8$) carrying possibly deleterious *CTSO* variations but without IA at the time of the study. In addition, we found a significant increase in the proportion of subjects with history of high blood pressure among IA carriers compared to unaffected individuals. High blood pressure history is a well-established environmental factor associated with the development of IA. Our results suggest, as described previously in familial cases with rare coding variants in *ANGPTL6*,[11] that rare coding variants in *CTSO* could promote IA formation in combination with other deleterious genetic or environmental factors such as high blood pressure, which would act either directly by mechanical effects on the vessel walls or indirectly by triggering inflammation.[28]

CTSO is one of the 11 cathepsins encoded in the human genome which constitute an important group of proteases that regulate numerous processes.[13] Cathepsins are highly expressed in intracellular acidic compartments such as endosomes and lysosomes. Loss of function mutations in their encoding genes cause very different syndromes in terms of clinical symptoms and disease progression, corresponding to either typical lysosomal storage diseases, or resulting from defective cleavage of specific protein substrates.[29] Cathepsins are also found in the cytoplasm, cell nucleus, cell membrane, and the extracellular space.[30] Extracellular cathepsins

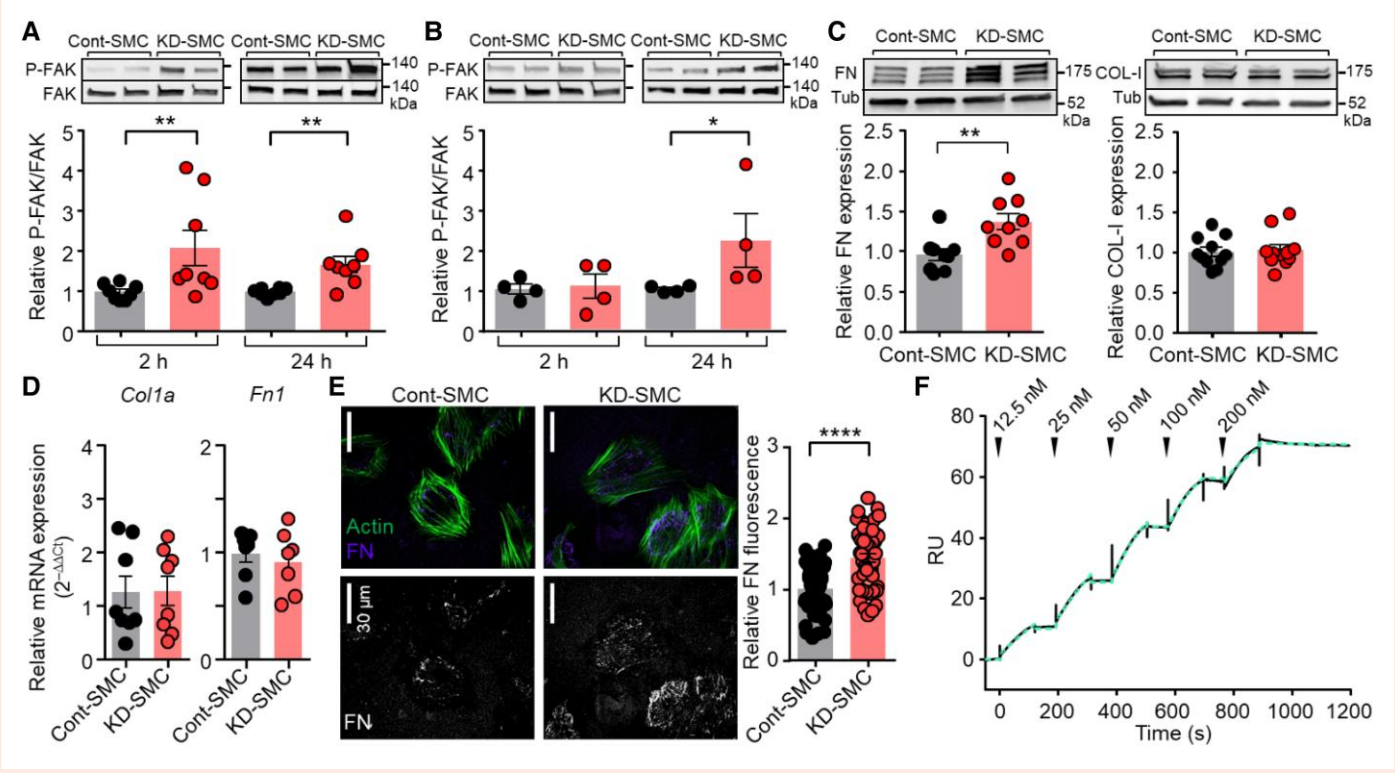

Figure 5 CTSO depletion in aortic VSMC stimulates FAK phosphorylation and FN expression. (*A* and *B*) Representative western blots showing the phosphorylation of FAK in Cont- and KD-SMC 2 and 24 h after seeding on FN matrix (*A*, $n = 8$ biological replicates) or directly on plastic (*B*, $n = 4$ biological replicates). Graphs show densitometric analysis of phospho-FAK in blots, relative to FAK expression. (*C*) Representative western blots showing the amount of FN and Col-I in Cont- and KD-SMC and corresponding quantification ($n = 9$ and 11 biological replicates, respectively). (*D*) RT–qPCR analysis of mRNA levels of Col1A, Fn1($n = 8$ and 7 biological replicates, respectively). Results were expressed relative to Cont-SMC and expressed as mean ± SEM (ns, Mann–Whitney test). (*E*) Representative immunofluorescent staining of human FN (purple) and phalloidin staining of actin fibres (green) in Cont- and KD-SMC (top images). Isolated FN staining is also shown (white, bottom images). SMC were seeded on human FN-coated surface. Quantification of FN has been made cell by cell (each dot represents a cell, $n = 4$ independent experiments). (*F*) Single-cycle kinetic SPR analysis of the interaction of FN with CTSO injected at the indicated concentrations. The green dotted line represents the kinetic global fit of the CTSO-FN interaction using 1:1 Langmuir model. (Results were expressed relative to Cont-SMC and presented as mean ± SEM; $^{*}P < 0.05$, $^{**}P < 0.01$, $^{****}P < 0.0001$; Mann–Whitney test.)

mediate ECM protein degradation (collagen, elastin, FN, laminin) and the release of ECM-bound factors, but also shed various membrane proteins including receptors, growth factors, cytokines, and adhesion proteins thereby influencing important cellular processes such as proliferation and differentiation, motility, cell–cell interaction, adhesion, inflammatory, and immune responses. Indeed, extracellular cathepsins are majorly up-regulated in pathological states and are implicated in a wide range of disorders including vascular remodelling and atherosclerotic diseases.[31] CTSB, CTSK, and CTSS have been found to be up-regulated in the wall of IA in an experimental model in rats, leading to the suggestion that deregulation and imbalance in the expression of cathepsins may contribute to the progression and rupture of IA.[32] Several observations in humans corroborate this idea. Genomic studies revealed up-regulation of *CTSB*, *CTSD*, *CTSZ* in IA walls compared to control arteries.[33–35] In addition, *CTSD* was shown to be more expressed in ruptured than in unruptured IA.[33] Immunohistochemical labelling of CTSB also indicated its higher expression in the wall of ruptured and unruptured IA.[36] Our data add CTSO to the family of cathepsins whose expression is dysregulated in aneurysms, highlighting the increased expression of CTSO, in particularly in the ECM, in ruptured human IA compared to unruptured IA.

At cell level, CTSO was found both in and around VSMC, and its extracellular release is stimulated by cell stretching, suggesting that its role as an extracellular protease in the arterial wall could be potentiated by high blood pressure and participate to the adaptive arterial remodelling induced by hypertension. The increase in CTSO expression observed in ruptured IA domes could thus result from the greater aneurysmal wall stretch induced by blood pressure in ruptured vs. unruptured IA.[37]

CTSO is defined as a ubiquitous protein but neither its peptidase activity nor its function had been characterized yet. Although we have not analysed the enzymatic activity of CTSO *in vitro* to directly demonstrate its ability to degrade FN, we provide a strong body of experimental evidence to support this hypothesis. Cell adhesion and FAK activation are potentiated by depletion of CTSO, both rapidly and late after VSMC seeding on exogenous FN coating, while only delayed stimulation of FAK activation was observed in CTSO-depleted VSMC seeded on plastic. These observations are consistent with a degradation of pericellular FN by CTSO, which instantaneously impaired cell-FN coating interaction in VSMC producing extracellular CTSO. When VSCM are seeded on plastic or on collagen, there is no difference in the initial adhesion speed between control and CTSO-depleted VSMC, and the effect of CTSO depletion is only visible at late time points, after the time necessary for the cells to self-produce FN with which they establish adhesions. This hypothesis is in agreement with the increase in the amount of FN in CTSO-deficient VSMC and is further supported by the strong immunofluorescence labelling of exogenous FN close to CTSO-depleted VSMC compared to its low intensity in CTSO-expressing cells. All these observations suggest that, as CSTB and CTSL do,[31] extracellular CTSO secreted by VSMC degrades FN. This suggestion is strengthened by the results obtained by SPR, which demonstrate

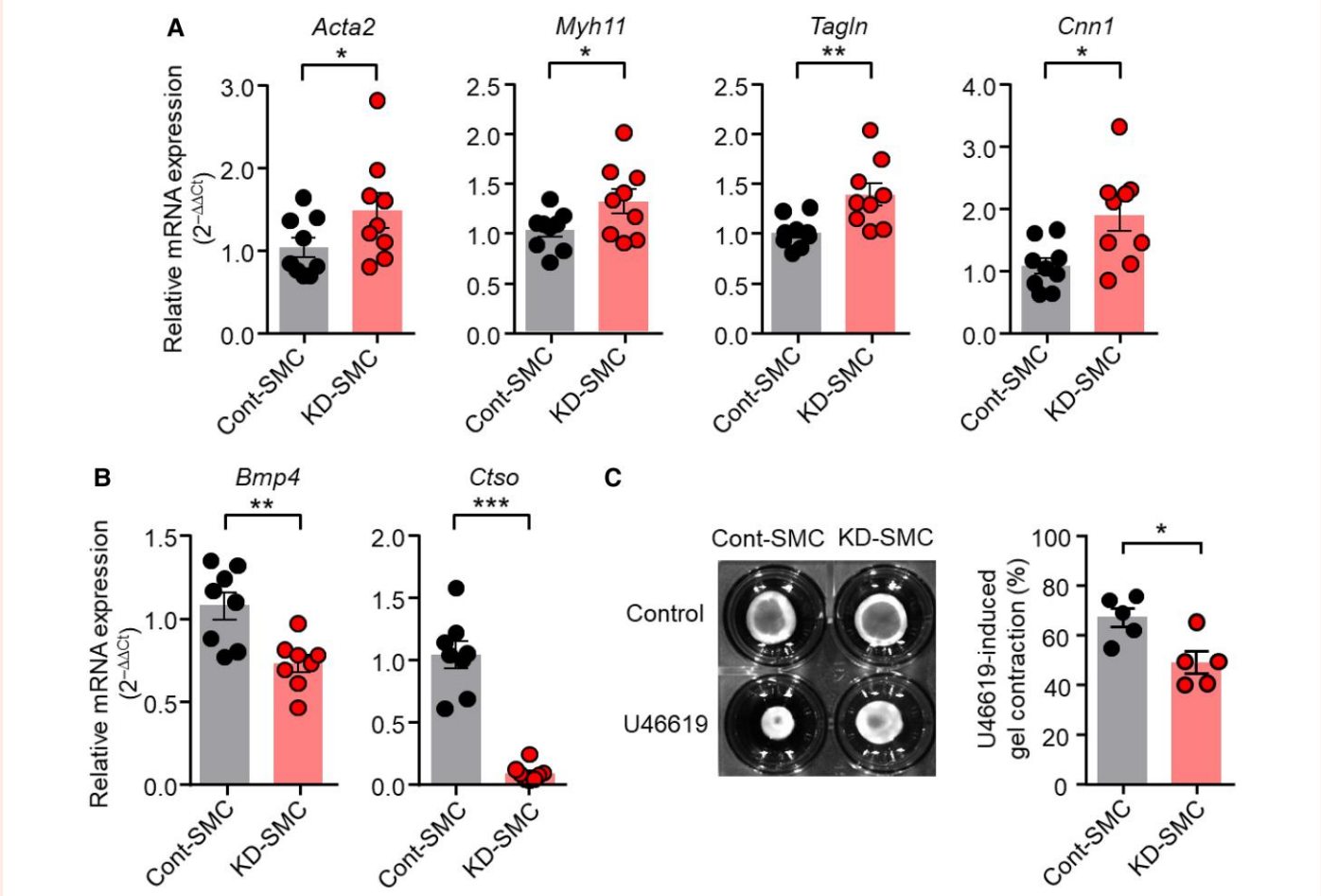

Figure 6 CTSO depletion in VSMC modulates contractile phenotype marker expression and contraction. (*A*, *B*) RT–qPCR analysis of mRNA levels of the SMC marker genes Acta2, Myh11, Talgn, Cnn1 (*A*); and Bmp4 and Ctso (*B*) in Cont- and KD-SMC ($n = 8$–9 biological replicates). Results were expressed relative to Cont-SMC and expressed as mean ± SEM; *$P < 0.05$, **$P < 0.01$, ***$P < 0.001$; Mann–Whitney test). (*C*) Representative images of Cont-SMC- and KD-SMC-seeded collagen gels 48 h after release with and without U46619 and quantification of U46619-induced gel contraction in Cont- and KD-SMC ($n = 5$ biological replicates). (Data are expressed as mean ± SEM; *$P < 0.05$; Mann–Whitney test).

the direct high-affinity interaction of CTSO with FN. Moreover, the observation that the expression of the two mutated proteins p.Val316Ile-CTSO and p.Ala43Val-CTSO, which are weakly secreted, mimics the effect of CTSO depletion by also inducing an increase in FN levels, is consistent with the degradation of FN by CTSO.

It is well established that adhesive properties to ECM drives VSMC stiffness,[38] and the level of activation of FAK signalling is related to VSMC stiffness.[39] In particular, VSMC focal adhesions to FN correlate with VSMC stiffness.[40] The strong stiffening of VSMC that we observed after CTSO depletion is therefore consistent with an increase in the ability of VSMC to form adhesions to FN due to the reduced degradation of FN in CTSO-depleted VSMC.

ECM composition and organization impact the physical interactions with VSMC, which play a major role in regulating their functions, including migration and differentiation. We observed that knocking-down CTSO reduced VSMC migration on FN. This result further supports a role of CTSO in promoting FN degradation, although additional mechanisms could also be involved such as degradation of other extracellular proteins or lysosomal degradation of FN-bound integrins known to be required for migration.[41] Regarding VSMC differentiation, CSTO depletion leads to increased expression of contractile phenotype marker genes such as *Acta2*. Interestingly, deletion or inhibition of cathepsin B, characterized as a FN-degrading protease[42] that is also up-regulated by cell stretching, also increases ACTA2 expression through an underlying mechanism that is still unknown.[43] Increased ACTA2 expression has been shown to contribute to VSMC stiffening,[44] suggesting that up-regulation of *Acta2* and possibly of the other contractile markers, could participate to the increase in VSMC stiffness induced by CTSO depletion. Although contractile markers were up-regulated, collagen gel contraction produced by KD-VSMC was reduced compared to Cont-VSMC. Whether this effect was related to the stiffness of VSMC induced by CTSO deletion could not be determined. Nevertheless, this possibility is supported by previous results obtained on VSMC from aged animals showing a similar association between increased stiffness[38] and reduced collagen gel contraction.[40,45]

Besides their contractile activity, VSMC produce ECM that allows adaptation to mechanical forces that act on the vessel wall while maintaining adequate wall pressure.[46,47] Thus, the composition, organization, and resulting interactions of ECM with VSMC are adjusted to the mechanical demands of the vessel wall through multiple and coordinated mechanisms. Among them, the fine-tuning of extracellular protease expression and activity plays a major role in ECM matrix reshaping.[31] Our present study proposes that CTSO, whose secretion is regulated by cell stretch, could be a new member of these ECM proteases involved in arterial wall adaptation to mechanical stress. Indeed, we have identified CTSO as a potential new player in arterial remodelling, regulating FN deposition and VSMC function. This role of CTSO is consistent with an increased susceptibility to IA associated with

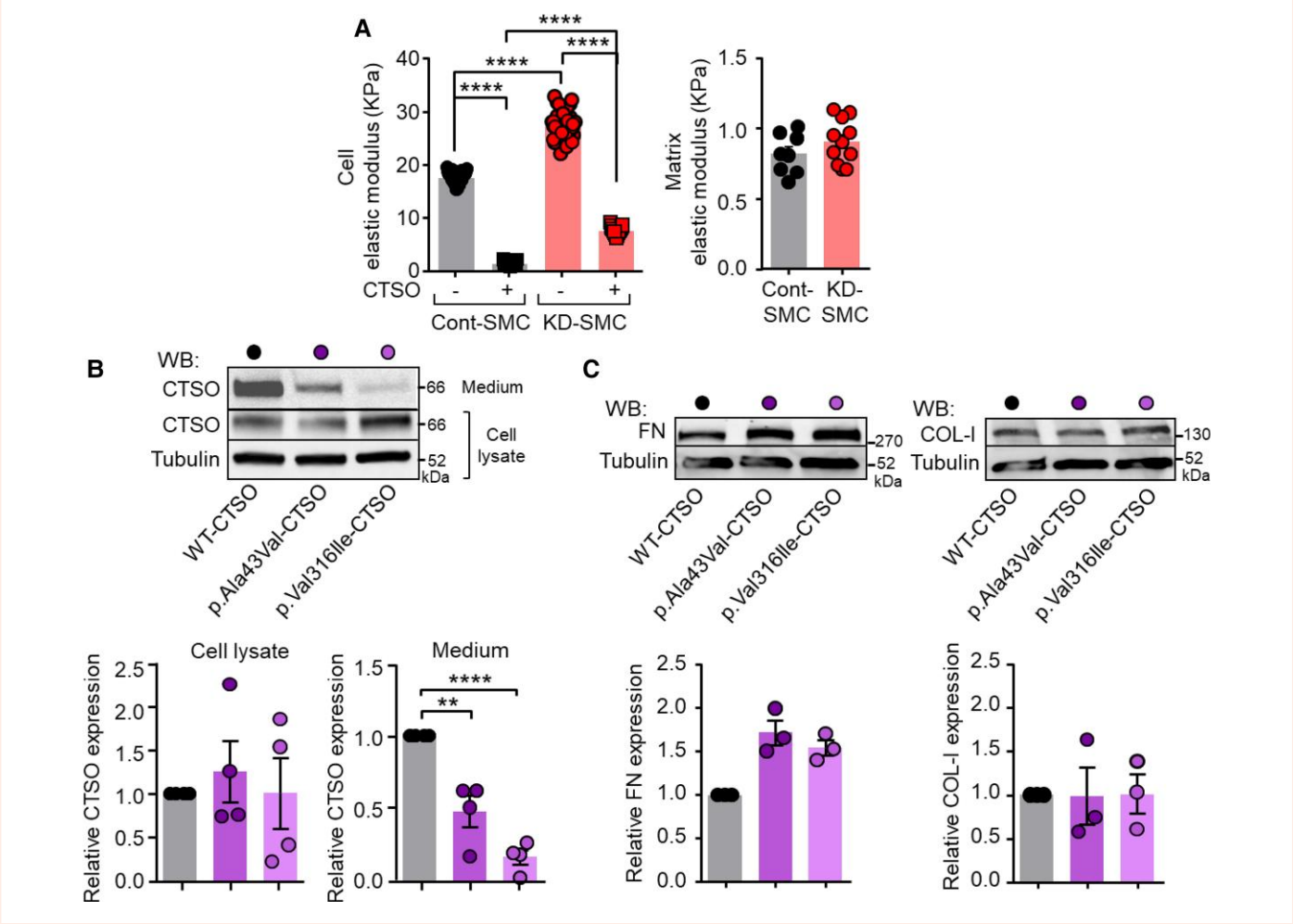

Figure 7 Effect of CTSO depletion and CTSO variant expression on cell stiffness and FN expression. (*A*) Atomic force microscopy determination of the elastic modulus of Cont- and KD-SMC, in the absence and presence of exogenous CTSO (200 ng/mL) (left), and their respective decellularized extracellular matrix (right) (each dot represents a cell or matrix sample, $n = 3$ independent experiments; dData are expressed as mean ± SEM; ****$P < 0.0001$; one-way *ANOVA* with Holm-Sidak post hoc test (left) and Mann–Whitney test (ns, right). (*B*) Representative western blots and quantification of CTSO protein expression measured in cell lysate and culture medium of NIH3T3 expressing WT-CTSO, p.Ala43Val-CTSO and p.Val316Ile-CTSO ($n = 4$ biological replicates). (*C*) Representative western blots and quantification of FN and Col-1 expression measured in WT-CTSO, p.Ala43Val-CTSO and p.Val316Ile-CTSO ($n = 3$ biological replicates). (Data are expressed as mean ± SEM; **$P < 0.01$ and ****$P < 0.0001$; One-sample *t* test.)

non-secreted c.128C > T *CTSO* and c.946G > A *CTSO* variants. We suggest that, by promoting increased FN deposition, VSMC-FN adhesion and VSMC stiffening, the p.Val316Ile-CTSO and p.Ala43Val-CTSO mutants affect the mechanical properties of the vessel wall and compromise the proper adaptation of the arterial wall to local hemodynamics, thereby favouring IA formation. It is noteworthy that similar features, namely faster adhesion to FN,[48] up-regulation of contractile marker expression and increased stiffness, have been described in Marfan syndrome VSMC,[49] a well-known genetic condition that predisposes to IA.[50]

4.1 Limitations

The demonstration of a direct causal relationship between the expression of CTSO variants and an alteration in VSMC function leading to a predisposition to IA has not been firmly established. A future study on the formation of IA in a model of CTSO-deficient mice or in mice expressing CTSO variants should provide an answer to this question. Although it is highly likely that CTSO function in VSMC is the same in humans and rodents, only rodent cells were analysed in this study, as it was not possible to obtain VSMC from human cerebral arteries of the circle of Willis.

Translational perspective

The mechanisms responsible for IA formation, growth, and rupture are mostly unknown. Identifying variants that increase the risk of IA could provide valuable insights into IA pathophysiology. Here, we identified rare missense variants in the *CTSO* gene associated with familial IA. We show that CTSO, whose secretion is enhanced by stretching, controls vascular smooth muscle cell (VSMC) adhesion, stiffness, and FN deposition. The disease-associated variants reduce CTSO secretion, promoting increased FN deposition. These findings support a pathogenic role of dysregulated VSMC-extracellular matrix interaction in IA and suggest the potential therapeutic interest of drugs targeting VSMC adhesion to extracellular matrix.

Supplementary material

Supplementary material is available at *Cardiovascular Research* online.

Authors' contributions

R.Bo., G.L., and R.R. designed the research. S.Ch., E.B., S.J., A.C., C.D., J.O., H.D., R.Bo., and ICAN Study group were involved in the recruitment of IA patients. S.M., B.R.K., and Ph.B., and provided human IA samples. Genetic data have been obtained and analyzed by R.Bl., S.Be., S.Bo., P.L., F.L., J.-FD., C.D., and R.R. M.F., M.-A.M., S.P.R.B., M.R., T.Q., M.B., and A.-C.V. performed CTSO function and expression experiments and analyzed the results. S.Cu. performed atomic force microscopy experiments. M.M. performed S.P.R. experiments. M.F. and R.Bl. shared the first-author position for their major contribution to the study: M.F. for functional analysis and R.Bl. for genetic analyses. G.L. and R.R. equally contributed to the management of the project, analysis and interpretation of the data and the writing of the manuscript. All authors discussed the results, red, commented and approved the final manuscript.

Acknowledgements

We are grateful to the genomics (GenoA), bioinformatics (BiRD), proteomics (Imp@ct), and microscopy core facilities (MicroPICell) (SFR Bonamy, Nantes, France), members of Biogenouest and IBISA, for their expert services. We also thank the Institut Français de Bioinformatique (IFB; ANR-11-INBS-0013) as well as the animal house facility (UTE) of Nantes Université. We would like to thank the Genome Aggregation Database (gnomAD) and the groups that provided exome and genome variant data to this resource. A full list of contributing groups can be found at http://gnomad.broadinstitute.org/about. We acknowledge the Center of Biological Resources (CHU Nantes, Hôtel-Dieu, CRB, Nantes, France) as well as Martine Le Cunff, Marie-France Le Cunff and the Clinical Investigation Center 1413 of Nantes for their assistance in managing the ICAN and PREGO biobanks.

Conflict of interest: none declared.

Funding

This work was supported by the French national research agency (ANR) (Programme d'Investissements d'Avenir ANR-16-IDEX-0007 [NeXT Initiative], ANR-21-CE17-0006 [to R.Bo.], ANR-21-CE14-0016 [to A.-C.V.], and ANR-15-CE17-0008-01 and ANR-23-CE14-0001 [to G.L.]), Fondation pour la Recherche Médicale (R22131NN—RAD22168NNA to GL), Institut de France—Académie des Sciences (Lamonica Award to G.L., supporting M.-A.M.), the Inserm and Regional Council of Pays de la Loire (to R.B.) and the local fund Genavie (to M.F. and R.R.). Study benefited of the framework of the AneuX project supported by grants from SystemsX.ch, and evaluated by the Swiss National Science Foundation (2014/261) exploiting the infrastructure previously elaborated during the @neurIST project supported by the 6th framework program of the European Commission (FP6-IST-2004-027703), as well as a research grant of the Swiss National Science Foundation (320030_231430 to B.R.K. and P.B.).

Data availability

All data needed to support the conclusions of this study are present in the paper and/or the Supplementary Material or are available via the corresponding authors upon reasonable request.

References

1. Vlak MH, Algra A, Brandenburg R, Rinkel GJ. Prevalence of unruptured intracranial aneurysms, with emphasis on sex, age, comorbidity, country, and time period: a systematic review and meta-analysis. *Lancet Neurol* 2011;**10**:626–636.
2. Nieuwkamp DJ, Setz LE, Algra A, Linn FH, de Rooij NK, Rinkel GJ. Changes in case fatality of aneurysmal subarachnoid haemorrhage over time, according to age, sex, and region: a meta-analysis. *Lancet Neurol* 2009;**8**:635–642.
3. Vlak MH, Rinkel GJ, Greebe P, Algra A. Risk of rupture of an intracranial aneurysm based on patient characteristics: a case-control study. *Stroke* 2013;**44**:1256–1259.
4. Bourcier R, Redon R, Desal H. Genetic investigations on intracranial aneurysm: update and perspectives. *J Neuroradiol* 2015;**42**:67–71.
5. Bakker MK, van der Spek RAA, van Rheenen W, Morel S, Bourcier R, Hostettler IC, Alg VS, van Eijk KR, Koido M, Akiyama M, Terao C, Matsuda K, Walters RG, Lin K, Li L, Millwood IY, Chen Z, Rouleau GA, Zhou S, Rannikmäe K, Sudlow CLM, Houlden H, van den Berg LH, Dina C, Naggara O, Gentric JC, Shotar E, Eugène F, Desal H, Winsvold BS, Børte S, Johnsen MB, Brumpton BM, Sandvei MS, Willer CJ, Hveem K, Zwart JA, Verschuren WMM, Friedrich CM, Hirsch S, Schilling S, Dauvillier J, Martin O; HUNT All-In Stroke; China Kadoorie Biobank Collaborative Group; BioBank Japan Project Consortium; ICAN Study Group; CADISP Group; Genetics and Observational Subarachnoid Haemorrhage (GOSH) Study investigators; International Stroke Genetics Consortium (ISGC); Jones GT, Bown MJ, Ko NU, Kim H, Coleman JRI, Breen G, Zaroff JG, Klijn CJM, Malik R, Dichgans M, Sargurupremraj M, Tatlisumak T, Amouyel P, Debette S, Rinkel GJE, Worrall BB, Pera J, Slowik A, Gaál-Paavola EI, Niemelä M, Jääskeläinen JE, von Und Zu Fraunberg M, Lindgren A, Broderick JP, Werring DJ, Woo D, Redon R, Bijlenga P, Kamatani Y, Veldink JH, Ruigrok YM. Genome-wide association study of intracranial aneurysms identifies 17 risk loci and genetic overlap with clinical risk factors. *Nat Genet* 2020;**52**:1303–1313.
6. Zhou S, Ambalavanan A, Rochefort D, Xie P, Bourassa CV, Hince P, Dionne-Laporte A, Spiegelman D, Gan-Or Z, Mirarchi C, Zaharieva V, Dupré N, Kobayashi H, Hitomi T, Harada K, Koizumi A, Xiong L, Dion PA, Rouleau GA. RNF213 is associated with intracranial aneurysms in the French-Canadian population. *Am J Hum Genet* 2016;**99**:1072–1085.
7. Santiago-Sim T, Fang X, Hennessy ML, Nalbach SV, DePalma SR, Lee MS, Greenway SC, McDonough B, Hergenroeder GW, Patek KJ, Colosimo SM, Qualmann KJ, Hagan JP, Milewicz DM, MacRae CA, Dymecki SM, Seidman CE, Seidman JG, Kim DH. *THSD1* (thrombospondin type 1 domain containing protein 1) mutation in the pathogenesis of intracranial aneurysm and subarachnoid hemorrhage. *Stroke* 2016;**47**:3005–3013.
8. Wu Y, Li Z, Shi Y, Chen L, Tan H, Wang Z, Yin C, Liu L, Hu J. Exome sequencing identifies LOXL2 mutation as a cause of familial intracranial aneurysm. *World Neurosurg* 2018;**109**:e812–e818.
9. Lorenzo-Betancor O, Blackburn PR, Edwards E, Vazquez-do-Campo R, Klee EW, Labbe C, Hodges K, Glover P, Sigafoos AN, Soto AI, Walton RL, Doxsey S, Bober MB, Jennings S, Clark KJ, Asmann Y, Miller D, Freeman WD, Meschia J, Ross OA. *PCNT* point mutations and familial intracranial aneurysms. *Neurology* 2018;**91**:e2170–e2181.
10. Yang X, Li J, Fang Y, Zhang Z, Jin D, Chen X, Zhao Y, Li M, Huan L, Kent TA, Dong JF, Jiang R, Yang S, Jin L, Zhang J, Zhong TP, Yu F. Rho guanine nucleotide exchange factor *ARHGEF17* is a risk gene for intracranial aneurysms. *Circ Genom Precis Med* 2018;**11**:e002099.
11. Bourcier R, Le Scouarnec S, Bonnaud S, Karakachoff M, Bourcereau E, Heurtebise-Chretien S, Menguy C, Dina C, Simonet F, Moles A, Lenoble C, Lindenbaum P, Chatel S, Isidor B, Genin E, Deleuze JF, Schott JJ, Le Marec H, Group IS, Loirand G, Desal H, Redon R. Rare coding variants in ANGPTL6 are associated with familial forms of intracranial aneurysm. *Am J Hum Genet* 2018;**102**:133–141.
12. Barak T, Ristori E, Ercan-Sencicek AG, Miyagishima DF, Nelson-Williams C, Dong W, Jin SC, Prendergast A, Armero W, Henegariu O, Erson-Omay EZ, Harmanci AS, Guy M, Gultekin B, Kilic D, Rai DK, Goc N, Aguilera SM, Gulez B, Altinok S, Ozcan K, Yarman Y, Coskun S, Sempou E, Deniz E, Hintzen J, Cox A, Fomchenko E, Jung SW, Ozturk AK, Louvi A, Bilguvar K, Connolly ES Jr, Khokha MK, Kahle KT, Yasuno K, Lifton RP, Mishra-Gorur K, Nicoli S, Gunel M. PPIL4 is essential for brain angiogenesis and implicated in intracranial aneurysms in humans. *Nat Med* 2021;**27**:2165–2175.
13. Reiser J, Adair B, Reinheckel T. Specialized roles for cysteine cathepsins in health and disease. *J Clin Invest* 2010;**120**:3421–3431.
14. Bourcier R, Chatel S, Bourcereau E, Jouan S, Marec HL, Daumas-Duport B, Sevin-Allouet M, Guillon B, Roualdes V, Riem T, Isidor B, Lebranchu P, Connault J, Tourneau TL, Gaignard A, Loirand G, Redon R, Desal H; ICAN Investigators. Understanding the pathophysiology of intracranial aneurysm: the ICAN project. *Neurosurgery* 2017;**80**:621–626.
15. Li H, Durbin R. Fast and accurate long-read alignment with Burrows-Wheeler transform. *Bioinformatics* 2010;**26**:589–595.
16. Poplin R, Ruano-Rubio V, DePristo MA, Fennell TJ, Carneiro MO, Van der Auwera GA, Kling DE, Gauthier LD, Levy-Moonshine A, Roazen D. Scaling accurate genetic variant discovery to tens of thousands of samples. bioRxiv 2018; doi: 10.1101/20178.
17. Karczewski KJ, Solomonson M, Chao KR, Goodrich JK, Tiao G, Lu W, Riley-Gillis BM, Tsai EA, Kim HI, Zheng X, Rahimov F, Esmaeeli S, Grundstad AJ, Reppell M, Waring J, Jacob H, Sexton D, Bronson PG, Chen X, Hu X, Goldstein JI, King D, Vittal C, Poterba T, Palmer DS, Churchhouse C, Howrigan DP, Zhou W, Watts NA, Nguyen K, Nguyen H, Mason C, Farnham C, Tolonen C, Gauthier LD, Gupta N, MacArthur DG, Rehm HL, Seed C, Philippakis AA, Daly MJ, Davis JW, Runz H, Miller MR, Neale BM. Systematic single-variant and gene-based association testing of thousands of phenotypes in 394,841 UK biobank exomes. *Cell Genom* 2022;**2**:100168.
18. Alves I, Giemza J, Blum MGB, Bernhardsson C, Chatel S, Karakachoff M, Saint Pierre A, Herzig AF, Olaso R, Monteil M, Gallien V, Cabot E, Svensson E, Bacq D, Baron E, Berthelier C, Besse C, Blanche H, Bocher O, Boland A, Bonnaud S, Charpentier E, Dandine-Roulland C, Ferec C, Fruchet C, Lecointe S, Le Floch E, Ludwig TE, Marenne G, Meyer V, Quellery E, Racimo F, Rouault K, Sandron F, Schott JJ, Velo-Suarez L, Violleau J,

Willerslev E, Coativy Y, Jezequel M, Le Bris D, Nicolas C, Pailler Y, Goldberg M, Zins M, Le Marec H, Jakobsson M, Darlu P, Genin E, Deleuze JF, Redon R, Dina C. Human genetic structure in Northwest France provides new insights into West European historical demography. *Nat Commun* 2024;**15**:6710.
19. Han L, Abney M. Identity by descent estimation with dense genome-wide genotype data. *Genet Epidemiol* 2011;**35**:557–567.
20. Morel S, Diagbouga MR, Dupuy N, Sutter E, Braunersreuther V, Pelli G, Corniola M, Gondar R, Jägersberg M, Isidor N, Schaller K, Bochaton-Piallat ML, Bijlenga P, Kwak BR. Correlating clinical risk factors and histological features in ruptured and unruptured human intracranial aneurysms: the Swiss AneuX study. *J Neuropathol Exp Neurol* 2018;**77**:555–566.
21. Gouëffic Y, Guilluy C, Guérin P, Patra P, Pacaud P, Loirand G. Hyaluronan induces vascular smooth muscle cell migration through RHAMM-mediated PI3K-dependent Rac activation. *Cardiovasc Res* 2006;**72**:339–348.
22. Ozguldez HO, Cha J, Hong Y, Koh I, Kim P. Nanoengineered, cell-derived extracellular matrix influences ECM-related gene expression of mesenchymal stem cells. *Biomater Res* 2018;**22**:32.
23. Cuenot S, Gélébart P, Sinquin C, Colliec-Jouault S, Zykwinska A. Mechanical relaxations of hydrogels governed by their physical or chemical crosslinks. *J Mech Behav Biomed* 2022;**133**:105343.
24. Zykwinska A, Makshakova O, Gélébart P, Sinquin C, Stephant N, Colliec-Jouault S, Perez S, Cuenot S. Interactions between infernan and calcium: from the molecular level to the mechanical properties of microgels. *Carbohydr Polym* 2022;**292**:119629.
25. Hedin U, Bottger BA, Forsberg E, Johansson S, Thyberg J. Diverse effects of fibronectin and laminin on phenotypic properties of cultured arterial smooth muscle cells. *J Cell Biol* 1988;**107**:307–319.
26. Yang P, Troncone L, Augur ZM, Kim SSJ, McNeil ME, Yu PB. The role of bone morphogenetic protein signaling in vascular calcification. *Bone* 2020;**141**:115542.
27. Matsukawa H, Shinoda M, Fujii M, Uemura A, Takahashi O, Niimi Y. Arterial stiffness as a risk factor for cerebral aneurysm. *Acta Neurol Scand* 2014;**130**:394–399.
28. Hudson JS, Hoyne DS, Hasan DM. Inflammation and human cerebral aneurysms: current and future treatment prospects. *Future Neurol* 2013;**8**:663–676.
29. Ketscher A, Ketterer S, Dollwet-Mack S, Reif U, Reinheckel T. Neuroectoderm-specific deletion of cathepsin D in mice models human inherited neuronal ceroid lipofuscinosis type 10. *Biochimie* 2016;**122**:219–226.
30. Yadati T, Houben T, Bitorina A, Shiri-Sverdlov R. The ins and outs of cathepsins: physiological function and role in disease management. *Cells* 2020;**9**:1679.
31. Liu CL, Guo J, Zhang X, Sukhova GK, Libby P, Shi GP. Cysteine protease cathepsins in cardiovascular disease: from basic research to clinical trials. *Nat Rev Cardiol* 2018;**15**:351–370.
32. Aoki T, Kataoka H, Ishibashi R, Nozaki K, Hashimoto N. Cathepsin B, K, and S are expressed in cerebral aneurysms and promote the progression of cerebral aneurysms. *Stroke* 2008;**39**:2603–2610.
33. Marchese E, Vignati A, Albanese A, Nucci CG, Sabatino G, Tirpakova B, Lofrese G, Zelano G, Maira G. Comparative evaluation of genome-wide gene expression profiles in ruptured and unruptured human intracranial aneurysms. *J Biol Regul Homeost Agents* 2010;**24**:185–195.
34. Pera J, Korostynski M, Krzyszkowski T, Czopek J, Slowik A, Dziedzic T, Piechota M, Stachura K, Moskala M, Przewlocki R, Szczudlik A. Gene expression profiles in human ruptured and unruptured intracranial aneurysms: what is the role of inflammation? *Stroke* 2010;**41**:224–231.
35. Shi C, Awad IA, Jafari N, Lin S, Du P, Hage ZA, Shenkar R, Getch CC, Bredel M, Batjer HH, Bendok BR. Genomics of human intracranial aneurysm wall. *Stroke* 2009;**40**:1252–1261.
36. Tyagi G, Srinivas D, Nanjaiah ND, Purushottam M, Somanna S, Santosh V, Jain S. Gene expression in intracranial aneurysms-comparison analysis of aneurysmal walls and extracranial arteries with real-time polymerase chain reaction and immunohistochemistry. *World Neurosurg* 2019;**130**:e117–e126.
37. Oliveira IL, Cardiff P, Baccin CE, Gasche JL. A numerical investigation of the mechanics of intracranial aneurysms walls: assessing the influence of tissue hyperelastic laws and heterogeneous properties on the stress and stretch fields. *J Mech Behav Biomed* 2022;**136**:105498.
38. Lacolley P, Regnault V, Avolio AP. Smooth muscle cell and arterial aging: basic and clinical aspects. *Cardiovasc Res* 2018;**114**:513–528.
39. Saphirstein RJ, Gao YZ, Jensen MH, Gallant CM, Vetterkind S, Moore JR, Morgan KG. The focal adhesion: a regulated component of aortic stiffness. *PLoS One* 2013;**8**:e62461.
40. Sehgel NL, Sun Z, Hong Z, Hunter WC, Hill MA, Vatner DE, Vatner SF, Meininger GA. Augmented vascular smooth muscle cell stiffness and adhesion when hypertension is superimposed on aging. *Hypertension* 2015;**65**:370–377.
41. Lobert VH, Brech A, Pedersen NM, Wesche J, Oppelt A, Malerød L, Stenmark H. Ubiquitination of alpha 5 beta 1 integrin controls fibroblast migration through lysosomal degradation of fibronectin-integrin complexes. *Dev Cell* 2010;**19**:148–159.
42. Buck MR, Karustis DG, Day NA, Honn KV, Sloane BF. Degradation of extracellular-matrix proteins by human cathepsin B from normal and tumour tissues. *Biochem J* 1992;**282**:273–278.
43. Nettesheim A, Shim MS, Dixon A, Raychaudhuri U, Gong H, Liton PB. Cathepsin B localizes in the caveolae and participates in the proteolytic cascade in trabecular meshwork cells. Potential new drug target for the treatment of glaucoma. *J Clin Med* 2020;**10**:78.
44. Qiu H, Zhu Y, Sun Z, Trzeciakowski JP, Gansner M, Depre C, Resuello RR, Natividad FF, Hunter WC, Genin GM, Elson EL, Vatner DE, Meininger GA, Vatner SF. Short communication: vascular smooth muscle cell stiffness as a mechanism for increased aortic stiffness with aging. *Circ Res* 2010;**107**:615–619.
45. Wheeler JB, Mukherjee R, Stroud RE, Jones JA, Ikonomidis JS. Relation of murine thoracic aortic structural and cellular changes with aging to passive and active mechanical properties. *J Am Heart Assoc* 2015;**4**:e001744.
46. Humphrey JD, Schwartz MA. Vascular mechanobiology: homeostasis, adaptation, and disease. *Annu Rev Biomed Eng* 2021;**23**:1–27.
47. Lin PK, Davis GE. Extracellular matrix remodeling in vascular disease: defining its regulators and pathological influence. *Arterioscler Thromb Vasc Biol* 2023;**43**:1599–1616.
48. Nolasco P, Fernandes CG, Ribeiro-Silva JC, Oliveira PVS, Sacrini M, de Brito IV, De Bessa TC, Pereira LV, Tanaka LY, Alencar A, Laurindo FRM. Impaired vascular smooth muscle cell force-generating capacity and phenotypic deregulation in Marfan syndrome mice. *Biochim Biophys Acta Mol Basis Dis* 2020;**1866**:165587.
49. Crosas-Molist E, Meirelles T, Lopez-Luque J, Serra-Peinado C, Selva J, Caja L, Gorbenko Del Blanco D, Uriarte JJ, Bertran E, Mendizabal Y, Hernandez V, Garcia-Calero C, Busnadiego O, Condom E, Toral D, Castella M, Forteza A, Navajas D, Sarri E, Rodriguez-Pascual F, Dietz HC, Fabregat I, Egea G. Vascular smooth muscle cell phenotypic changes in patients with Marfan syndrome. *Arterioscler Thromb Vasc Biol* 2015;**35**:960–972.
50. Kim JH, Kim JW, Song SW, Ahn SJ, Park M, Park SK, Suh SH. Intracranial aneurysms are associated with Marfan syndrome: single cohort retrospective study in 118 patients using brain imaging. *Stroke* 2021;**52**:331–334.